Structures of *Tetrahymena*'s respiratory chain reveal the diversity of eukaryotic core metabolism

Long Zhou[1,†], **María Maldonado**[2,†], **Abhilash Padavannil**[2], **Fei Guo**[3], **James A. Letts**[2,*]

[1]Department of Biophysics and Department of Critical Care Medicine of Sir Run Run Shaw Hospital, Zhejiang University School of Medicine, Hangzhou 310058, China.

[2]Department of Molecular and Cellular Biology, University of California, Davis, CA 95616, USA.

[3]BIOEM Facility, University of California, Davis, CA 95616, USA.

Abstract

Respiration is a core biological energy-converting process whose last steps are carried out by a chain of multi-subunit complexes in the inner mitochondrial membrane. To probe the functional and structural diversity of eukaryotic respiration, we examined the respiratory chain of the ciliate *Tetrahymena thermophila* (Tt). Using cryo-electron microscopy on a mixed sample, we solved structures of a supercomplex between Tt-complex I (CI) and Tt-CIII$_2$ (Tt-SC I+III$_2$) and a structure of Tt-CIV$_2$. Tt-SC I+III$_2$ (~2.3 MDa) is a curved assembly with structural and functional symmetry breaking. Tt-CIV$_2$ is a ~2.7 MDa dimer with over 50 subunits per protomer, including mitochondrial carriers and a TIM8$_3$-TIM13$_3$-like domain. Our structural and functional study of the *T. thermophila* respiratory chain reveals divergence in key components of eukaryotic respiration, expanding our understanding of core metabolism.

Cellular respiration is an essential metabolic process that provides chemical energy (ATP) to all free-living eukaryotes. The final energy-converting steps of cellular respiration are carried out by the mitochondrial oxidative phosphorylation electron transport chain (mETC), which transfers electrons from reduced metabolites such as NADH or succinate to the final electron acceptor, O$_2$. The mETC, located in the inner mitochondrial membrane (IMM), is composed of four protein complexes: NADH-ubiquinone (Q) oxidoreductase (complex I,

Corresponding author. jaletts@ucdavis.edu.
†These authors contributed equally to this work.

SUPPLEMENTARY MATERIALS

science.org/doi/10.1126/science.abn7747

Materials and Methods

Supplementary Text

Figs. S1 to S22

Tables S1 to S7

References (65–102)

Movies S1 and S2

CI), succinate dehydrogenase (complex II, CII), dimeric ubiquinol (QH_2)-cytochrome c (cyt c) oxidoreductase (complex III_2, $CIII_2$) and cytochrome c oxidase (complex IV, CIV). By coupling the energetically favorable electron transfer reactions to H^+ pumping across the IMM, the mETC complexes CI, $CIII_2$ and CIV establish a proton motive force (pmf) that is used by the ATP synthase complex (complex V, CV) to synthesize ATP (1). In all eukaryotes investigated, the mETC complexes are found both individually and as parts of higher order supercomplexes (SCs) of defined stoichiometry (2), including SC I+III_2, SC I+III_2+IV and SC III_2+$IV_{(2)}$ (3). CIV and CV are also commonly found as dimers (CIV_2 and CV_2) (4, 5) or, in the case of CV, higher-order arrays (6–9).

Although the catalytic mechanisms of the individual mETC complexes are likely conserved across species, some structural differences have been observed between model organisms. Each mETC complex can be split into core subunits – essential for catalysis and conserved from the bacterial homologs – and accessory subunits – important for the assembly and activity of the complexes but not universally conserved (10, 11). CI is composed of 14 core subunits, arranged into two "arms" of an "L"-shape, universally conserved in the model eukaryotes with known structures, covering the Opisthokont (fungi (12) and metazoan (13)) and Archaeplastida (red/green algae and plants (14–16)) clades. However, each structure of CI has a variable set of 31–37 accessory subunits, some of which are shared across all known examples of eukaryotic CI and some of which are only found in a specific branch of the eukaryotic tree of life (table S1) (17). For the other H^+-pumping complexes of the mETC ($CIII_2$ and CIV) much less compositional variability has been observed between the characterized examples from opisthokonts (4, 18, 19) and archaeplastidans (20) (tables S2 and S3). Although the biochemical and structural characterization of eukaryotic CI, $CIII_2$ and CIV has been limited to model organisms of the Opisthokonta and Archaeplastida clades, mitochondrial CV has been structurally characterized from a broader array of eukaryotes, including not only opisthokonts (5, 21) and archaeplastidans (22), but also kinetoplastids (23) and euglenids (24) (euglenozoans), as well as ciliates (9) and apicomplexans (8) (alveolates). These structures have revealed a broad diversity in subunit composition and higher-order organization of CV, correlated with differences in the organisms' IMM morphology (7, 8, 23, 25). The diversity in CV and the IMM morphology across eukaryotic clades suggests that the limited diversity seen in CI, $CIII_2$ and CIV may be due not to their essential nature but, instead, to the limited model eukaryotes in which they have been biochemically and structurally investigated.

Early functional characterization of the model ciliate *Tetrahymena thermophila* led to the conclusion that its mETC lacked CIV and contained a distinct terminal oxidase instead (26). However, the identification of *T. thermophila* homologs of CIV core subunits COX1 and COX2 (but not COX3) in the mitochondrial genome (27) and the discovery that *T. thermophila* possesses an acidic rather than a basic cyt c (28) indicated that, although *T. thermophila* does possess a CIV homolog, the complex has functionally diverged. Similarly, some but not all the core subunits of CI and $CIII_2$ were identified in the *T. thermophila* mitochondrial genome (27) and proteome (29). This is in line with proteomic studies of $CIII_2$ and CIV composition in alveolates *Toxoplasma gondii* and *Plasmodium falciparum*, which show a significant compositional divergence of these respiratory complexes relative to organisms with known structures (30, 31). Furthermore, unlike the disc-shaped cristae of

opisthokonts and archaeplastidans, the cristae of the ciliates and other alveolates are tubular (7). Given these functional, sequence, compositional and morphological differences with previously studied organisms, *T. thermophila* is an ideal system to examine the diversity, evolution and conserved aspects of mETC complexes.

The *T. thermophila* mETC requires a divergent cyt *c*

To examine the functional consequences of the acidic vs. basic charge flip of *T. thermophila*'s cyt *c* (Tt-cyt *c*), we characterized isolated mitochondrial membranes from *T. thermophila*, mammals (*Sus scrofa*, pig) and plants (*Vigna radiata*, mung bean) using both mammalian cyt *c* purified from horse heart (*Equus ferus*, equine, Eq-cyt *c*), and heterologously expressed Tt-cyt *c* (fig. S1, A to E) (32). Spectroscopic activity assays for SC I+III$_2$ showed NADH-cyt *c* oxidoreduction using Eq-cyt *c* for all three species (fig. S1, F to J). However, CIV activity assays showed that, whereas mammalian and plant mitochondrial membranes readily oxidize reduced Eq-cyt *c*, no cyt *c* oxidation could be detected from *T. thermophila* mitochondrial membranes (Fig. 1A). Conversely, using the recombinant Tt-cyt *c*, only the *T. thermophila* mitochondrial membranes showed cyanide-sensitive cyt *c* oxidation activity (Fig. 1A). These data establish that *T. thermophila* possesses a CIV that has functionally diverged from those of opisthokonts and archaeplastidans (fig. S1, K to M).

High resolution structures of the respiratory chain from a single mixed sample

To better understand the functional divergence of the *T. thermophila* mETC complexes, we extracted them from mitochondrial membranes using digitonin, stabilized them in amphipathic polymer A8–35 and enriched them using sucrose gradient ultracentrifugation and size-exclusion chromatography (fig. S2). We then obtained the structures of Tt-CI, Tt-CIII$_2$ and Tt-CIV$_2$ from a single mixed sample by single-particle cryogenic electron microscopy (cryoEM) (Fig. 1, B to D, figs. S3 to S6, and tables S4 to S7). Our dataset also allowed us to obtain a high-resolution reconstruction of Tt-CV$_2$ (fig. S5 and supplementary text), whose structure has been previously characterized (9). Thus, the current study reconstructed an entire metabolic pathway (NADH to ATP) involving 277 proteins in three multi-MDa complexes from a single sample (Fig. 1B).

Tt-CI and Tt-CIII$_2$ form a supercomplex (Tt-SC I+III$_2$) (Fig. 1C and movie S1) while Tt-CIV forms a dimer (Tt-CIV$_2$) (Fig. 1D and movie S2), resolved to nominal resolutions of 2.6 Å and 3.0 Å respectively (figs. S3 to S6). The subunit composition of the complexes was determined from the cryoEM density maps (33) and confirmed by mass spectrometry analysis (tables S5 to S7). Using this approach, we were able to structurally identify 70 proteins previously annotated as putative or uncharacterized in the sequence databases. Tt-SC I+III$_2$ is composed of 91 protein subunits and has an overall mass of ~2.3 MDa (Fig. 1C and tables S5 and S6), ~900 kDa larger than the mammalian SC I+III$_2$ (67 subunits, 1.4 MDa) (34). The position and relative orientation of CI and CIII$_2$ in Tt-SC I+III$_2$ are analogous to the conserved orientation other eukaryotes (fig. S7A) (2), suggesting either a common SC ancestor or convergent evolution across Opisthokonta, Archaeplastida and Alveolata. In contrast to mammalian, yeast and plant CIV with 10–14 subunits (table S3) (4,

20, 35), Tt-CIV$_2$ has an overall mass of ~2.7 MDa with over 52 subunits per protomer, (Fig. 1D and tables S3 and S7).

Unlike the planar architecture of previously described supercomplexes (fig. S7B) (34), Tt-SC I+III$_2$ and Tt-CIV$_2$ are curved assemblies (Fig. 1B), as demonstrated by the orientation of individual complexes (fig. S7, B to D) and the modeled lipids (Fig. 1B). When Tt-SC I+III$_2$, Tt-CIV$_2$ and Tt-CV$_2$ structures were fit into a circular membrane corresponding to the known diameter of the tubular ciliate cristae (~40 nm) (7), the modeled lipids (Fig. 1B) and hydrophobic regions of the proteins (fig. S7, B to D) matched the predicted curvature of a ~3 nm bilayer. The mETC complexes thus contribute to the tubular morphology of the ciliate cristae via specific structural features that are not conserved in opisthokonts or archaeplastidans.

Tt-CI has a fragmented core and 51 accessory subunits

Unlike all previous structurally characterized CIs, three core membrane subunits of Tt-CI responsible for Q binding and H$^+$-pumping (ND1, ND2 and ND5) are each split into two subunits, making a total of 17 core subunits across both CI arms (Fig. 2A). Comparison of the structures of these split subunits with the core subunits of other CIs indicate that subunits ND1A and ND1B, ND2A (formerly YMF65) and ND2B (formerly ND2), and ND5A and ND5B (formerly YMF57) come together to form structural elements equivalent to ND1, ND2 and ND5, respectively (fig. S8A and supplementary text) (27). Our structure also confirmed the previous speculative assignments of YMF62 and YMF58 as core subunits ND6 and ND4L respectively (table S5) (27). Notwithstanding these differences, the relative locations of the flavin mononucleotide (FMN) co-factor and eight ironsulfur clusters of the peripheral arm are highly conserved (fig. S8B). In addition, the hydrophilic axis along the center of the membrane is maintained, although it now involves residues of the additional subunits ND1B and ND2B (Fig. 2B). Furthermore, the positions of key Q reduction site loops (NDUS7, NDUS2 β1-β2, ND1A TMH5–6, ND3 TMH1–2, ND6 TMH3–4) are well resolved (Fig. 2C) and consistent with positions of the equivalent loops in the mammalian "closed" state structure (fig. S9) (13).

Among the 51 accessory subunits present in Tt-CI (Fig. 2D), 26 have homologs in all other known eukaryotic CIs, 5 subunits have homologs outside of the alveolates and 20 are newly identified here as CI subunits (fig. S10, tables S1 and S5, and supplementary text). The conservation of subunits across Opisthokonta, Archaeplastida and Alveolata defines a minimal set of 31 accessory subunits present in CI of the last eukaryotic common ancestor (LECA) (fig. S10 and table S1). As seen in the archaeplastidan structures (14–16), Tt-CI contains a γ-carbonic anhydrase (γCA) domain composed of three γCA subunits (Fig. 2E). Unlike vascular plants (14, 16) but like the non-photosynthetic alga *Polytomella* (15), none of the Tt-γCA subunits (NDUCA1–3) retain their catalytic Zn^{2+} coordinating residues (fig. S11, A and B). The ferredoxin bridge domain connecting the peripheral and membrane arms in plant and algal CI (15) is also present in Tt-CI (Fig. 2F). In addition to the *T. thermophila* homologs of the ferredoxin-like subunit (NDUFX), the acyl-carrier protein subunit (NDUAB1-α) and accessory subunit NDUA6, the bridge in Tt-CI is further stabilized by a J-domain subunit (coined NDUJ1) and the extended C terminus of NDUCA3

(Fig. 2F). Whereas the plant and algal CI-FDX has lost its ability to coordinate an iron-sulfur co-factor (15), we observe clear density for a 2Fe2S cluster in *T. thermophila*'s NDUFX (figs. S7E and S11, C and D) indicating that it may be a functional redox cofactor.

Tt-CI lacks an A/D transition and has crowded Q-site loops

Structural analyses of yeast and mammalian CI have revealed that the complex adopts distinct "open" and "closed" conformational states characterized by a global change in the angle between the two arms, as well as order-to-disorder rearrangements of the Q-reduction site loops (e.g., the ND3 TMH1–2 loop, Fig. 3A) and an α-helix to π-bulge conversion in ND6 TMH3 (fig. S9) (13, 34, 36, 37). These conformational changes have been proposed to be part of CI's coupling mechanism between Q reduction and H^+ pumping (13, 38). However, yeast and mammalian CIs are also capable of undergoing an "active-to-deactive" (A/D) transition, whereby CI enters an off-pathway deactive (D) state that is incapable of catalytic turnover (39). Therefore, it has been controversial whether the structural rearrangements of the open and closed states (fig. S9) are central to CI turnover or represent A and D states (13, 40). The A/D transition is not a universal feature of CI, as several bacterial and invertebrate CIs lack a D state (39). Structural characterization of a CI lacking the A/D transition would address this controversy: if these structural rearrangements were required for CI's catalytic mechanism, they should be possible even in CIs that lack an A/D transition.

Upon entering the D state, e.g., by incubating the mitochondrial membranes at 37°C in the absence of substrate, a conserved cysteine residue in CI's ND3 TMH1–2 loop (Cys45[ND3] in *T. thermophila*, Fig. 3, A and B) becomes accessible to modification by N-ethyl maleimide (NEM) (41). NEM modification of this cysteine traps CI in the D state and reduces overall activity (fig. S12). The detrimental effect of NEM on mammalian CI activity can be prevented by preactivating the complex with a small amount of NADH substrate (Fig. 3C). This outcome can be understood structurally: when mammalian CI is in the "closed" state, the ND3 TMH1–2 loop is ordered and the cysteine residue (Cys39[ND3] in *O. aries*) is buried in the structure, whereas when CI is in the "open" state the ND3 TMH1–2 is disordered and the cysteine is accessible to NEM (Fig. 3B). A similar effect can be seen with the addition of Mg^{2+}, which is known to inhibit the A/D transition in mammals and yeast (Fig. 3D) (39). When treated identically to the mammalian sample to induce entry into the D state (i.e., incubation without substrate at 37°C for 10–20 min), the CI activity of *T. thermophila*'s mitochondrial membranes were insensitive to NEM or Mg^{2+} (Fig. 3, E and F). These data indicate that, like bacteria and invertebrates (39), Tt-CI does not possess an A/D transition. Furthermore, in Tt-CI, the presence of additional *T. thermophila*-specific subunits (NDUJ1, NDUTX and NDUCA3) and of extensions in NDUA6 and NDUA9 leads to crowding of the region surrounding the ND3 TMH1–2 loop (Fig. 3G). Due to this crowding, any conformational changes of the ND3 TMH1–2 loop during the catalytic cycle would require rearrangements of the surrounding structure. For example, the observed position of Tt-CI's ND3 TMH1–2 loop conflicts with the "up" position of the ND1 TMH5–6 loop seen in the *O. aries* complex I bound to NADH (Fig. 3H) (12). Thus, if the "up" position of the loop is a conserved on-pathway state, the ND3 TMH1–2 loop and the surrounding subunits must undergo large (>5 Å) displacements during turnover. Disulfide crosslinking of

the ND3 TMH1–2 loop has been shown to uncouple Q reduction and H$^+$ pumping in yeast CI (*Y. lipolytica*) (42), indicating that conformational flexibility in this region is essential for redox-driven H$^+$ pumping. Given the crowded environment of this loop in Tt-CI, explicit disordering of this loop during turnover is unlikely. Thus, Tt-CI is an important model system in which to study these coordinated conformational changes during the CI catalytic cycle.

Although the angle between Tt-CI's membrane and the peripheral arm are more similar to some "open" states (fig. S9, E to H), given Tt-CI's well-ordered Q-reduction site loops (Fig. 2C) and the lack of a π-bulge in ND6 TMH3 (fig. S9D), our structure corresponds most closely with the "closed" state of mammalian and yeast CIs. This confirms that the "closed" state is an active state of the enzyme (12, 37, 38). Unlike the CI structures from opisthokonts and archaeplastidans (12, 13, 15, 34), resting Tt-CI does not contain structural classes with distinct angles between the membrane and peripheral arms, i.e., open and closed states. Given the multiple additional subunits that bridge the two arms of Tt-CI (Fig. 2, E and F), large conformational changes between the peripheral and membrane arms are unlikely. Therefore, we can conclude that both the ND6 TMH3 π-bulge and the open state of CI with disordered Q-site loops are features of the D state of the enzyme and not related to the conserved coupling mechanism.

Tt-SC I+III$_2$ breaks the symmetry of Tt-CIII$_2$

Although the overall arrangement of Tt-SC I+III$_2$ is like the mammalian supercomplex (fig. S7A) (34), the interactions between Tt-CI and Tt-CIII$_2$ are more extensive. Whereas mammals show one interaction site in the matrix and one in the IMM involving six subunits (3), Tt-SC I+III$_2$ possesses three matrix bridges (sites 1–3), IMM interactions (site 4) and an IMS bridge (site 5; Fig. 4A) involving 10 Tt-CIII$_2$ subunits and 11 Tt-CI subunits (fig. S13 and supplementary text). Two of *T. thermophila*'s matrix sites —the "thioredoxin/J bridge" and the "toe bridge"—are formed by Tt-CI subunits not seen in other organisms (Fig. 4, B and C). The additional bridges in the matrix wedge between Tt-CI and Tt-CIII$_2$ and push their matrix domains apart. Concomitantly, novel interactions in the IMS, including a shared Zn^{2+} coordination between NDUA11 and UQCRH (fig. S13I), pull the complexes together. Overall, these interactions splay Tt-SC I+III$_2$ in line with the IMM curvature (Fig. 1B and fig. S7B). Furthermore, ordered lipids bridge the Tt-CI and Tt-CIII$_2$ interface at the matrix and IMS leaflets of the membrane (Fig. 4, D and E).

Although divergent in sequence, each Tt-CIII protomer is composed of the 10 known CIII subunits seen in other eukaryotic species (Fig. 4, F and G) and 2 unidentified short chains (figs. S14 and S15 and supplementary text). CIII$_2$ is a symmetric dimer, but the structures of mammalian supercomplexes provided initial indications that CIII$_2$ may be symmetry-broken in higher-order assemblies (34, 43, 44). The structure of Tt-CIII$_2$ displays extensive structural and functional symmetry breaking caused by its interaction with Tt-CI, including differential flexibility or occupancy of several subunits (Fig. 4H). The UQCRFS1 head domain adjacent to the CI Q reduction site lacks clear cryoEM density due to highly flexibility, whereas the head domain proximal to the "toe bridge" (Fig. 4B) is restricted by its proximity to Tt-CI's NDUB8, leading to clear density (Fig. 4, H and I). Given that the

swinging motion of the UQCRFS1 head domain is essential for CIII$_2$'s electron transfer from QH$_2$ to cyt c_I (45), we conclude that the UQCRFS1 proximal to the toe bridge is likely not functional. Thus, only the Tt-CIII protomer adjacent to the source of QH$_2$ on CI is capable of QH$_2$ oxidation. The symmetry breaking of Tt-CIII$_2$ is further demonstrated by the widening of the distance between the two catalytic b_L hemes (Fig. 4, J and K). In bacteria, yeast, plants and mammals, the CIII$_2$ dimer arranges the b_L hemes within direct electron-transfer distance (~11 Å) (20, 46); a similar distance is also conserved in the distantly related cytochrome b_6f complex of the photosynthetic ETC (Fig. 4J) (47). Direct electron transfer between the b_L hemes is known to occur and thought to play a role in the catalytic mechanism of CIII$_2$ (48). In contrast, in *T. thermophila* the supercomplex interactions (Fig. 4A) and the membrane curvature (Fig. 1B) widen the distance and change the relative tilt between the two Tt-CIII protomers, resulting in an increased gap between the b_L hemes, placing them beyond rapid electrontransfer distance (Fig. 4J).

The symmetry breaking of the Rieske head domains and the increased distance between the b_L hemes would result in the inability of the Tt-CIII COB subunit distal to the Tt-CI Q site to accept electrons, leading to the functional specialization of the two Q cavities (Fig. 4L). In a symmetric CIII$_2$, each Q binding cavity contains a QH$_2$-oxidizing site (Q$_P$) near the IMS and a Q-reducing site (Q$_N$) near the matrix, each provided by the opposite COB protomer (34). Direct electron transfer across protomers means that there are four possible electron pathways between the Q$_P$ and Q$_N$ sites during the Q cycle (49). The symmetry breaking of the Rieske head domains and increased b_L-heme distance in the Tt-SC I+III$_2$ structure remove three possible pathways. The only possible electron transfer path is from the Q$_P$ site of the Q cavity adjacent to Tt-CI's Q tunnel (the source of QH$_2$) to the Q$_N$ site of the same COB subunit in the opposite Q cavity (Fig. 4L). This leads to the specialization of the Q cavities in the Q cycle: the one adjacent to the source of QH$_2$ would be responsible for QH$_2$ oxidation and the other one, for Q reduction (Fig. 4L). Although this functional symmetry breaking has been previously proposed for mammalian SC I+III$_2$ (3, 34), the unprecedented asymmetry in Tt-SC I+III$_2$ reveals how the CIII$_2$ electron transfer pathways are limited within the supercomplex, validating previous predictions and confirming a key physiological function of supercomplex formation. Furthermore, the large number of contacts between Tt-CI and Tt-CIII$_2$, the adaptation of the supercomplex to the high membrane curvature and the lack of biochemical detection of individual Tt-CI on BN-PAGE gels (fig. S2E) all suggest that Tt-SC I+III$_2$ is the minimal organization of Tt-CI, i.e., no free Tt-CI is present in *T. thermophila* mitochondrial membranes. While obligatory supercomplexes have been seen between CIII$_2$ and CIV in actinobacteria (50), none have been previously observed in eukaryotes.

Tt-CIV$_2$ is a 2.7 MDa dimer with a deep, charge swapped cytochrome c crater

Tt-CIV$_2$ is unlike any cytochrome *c* oxidase of known structure (fig. S16A). With its 2.7 MDa size (1.35 MDa per protomer), it surpasses CI as the largest complex of the mETC (Fig. 1D). Its subunits include the 3 universally conserved core catalytic subunits, 6 accessory subunits found in other eukaryotes and 44 accessory subunits not seen in other

CIV structures (fig. S17, table S3, and supplementary text). Although the transmembrane domains and catalytic co-factors are conserved (fig. S18), all three Tt-CIV core subunits (COX1–3) contain large extensions and insertions (Fig. 5A). The sequence and structural divergence of COX3 (formerly YMF68) is such that it previous identification by homology was not possible (27). In the IMS, the core subunits' extensions form the cyt c binding 'crater' (Fig. 5B) together with several accessory subunits (fig. S19A). Analogous to Tt-cyt c (fig. S1, A and B), the Tt-CIV crater shows a flipped surface electrostatic potential relative to bacteria, opisthokonts and plants (Fig. 5, B to D, and supplementary text). This 'swapped' charge property between Tt-CIV$_2$ and Tt-cyt c (fig. S20) explains why electron transfer cannot happen between mammalian cyt c and Tt-CIV$_2$ but can happen between mammalian cyt c and plant CIV (Fig. 1A).

The proton-conductance pathways ("K-, D- and H-channels channels") (51) that provide the chemical and pumped protons to CIV also show differences in *T. thermophila*. Although a critical proton acceptor in the D-channel is conserved (Glu393^{COX1}), a key threonine of the K-channel important for turnover in bacterial, archaeplastidan and opisthokont CIV (T316^{COX1} in yeast) (52) is replaced by a non-protonatable alanine in Tt-COX1 (A466^{COX1}) (fig. S19B). Thus, the Tt-CIV$_2$ K-channel either follows a different path or is not operational. Similarly, a key proton acceptor (Asp51^{COX1} in bovine CIV) (53) and a conserved cation (18) are missing in Tt-CIV$_2$'s H-channel (fig. S19B), suggesting a function as a dielectric regulator rather than as a proton channel in Tt-CIV$_2$ (51). Other key residues for O_2 access to the binuclear center and electron transfer from cyt c are conserved (fig. S19, C and D, and supplementary text).

Tt-CIV$_2$ incorporates mitochondrial carriers and a small-TIM-like hexamer

Most of Tt-CIV's 44 accessory subunits remained uncharacterized or putative in the *T. thermophila* genome (fig. S17E) (29), with only 13 showing recognizable folds (fig. S17C). These subunits include three mitochondrial carriers (COXMC1–3; Fig. 5E), a hexameric TIM8$_3$-TIM13$_3$ chaperone-like domain (COXTIM1–6) in the IMS, a β-propeller domain protein (COXBP), an acyl carrier protein (COXAC) and a [2Fe2S]-MitoNEET-like domain protein (COXFS; Fig. 5F) with two FeS cofactors in the matrix (fig. S21 and supplementary text). Tt-CIV$_2$ also contains three mitochondrially encoded subunits (YMF67, YMF70 and YMF75) that do not have homologs in any other known CIV structures (Fig. 5G) including the ancestral α-proteobacterial CIV (54), indicating that the ciliate mitochondrial genome has gained new genes. Additionally, there are several posttranslational modifications in accessory subunits visible in the cryoEM maps (fig. S18 and supplementary text).

Mitochondrial carriers, or solute carrier family 25 (SLC25), are essential proteins that carry solutes into and out of the mitochondrial matrix (55). Although direct interaction between carriers and respiratory complexes has been proposed (56), this has remained controversial. The structure of Tt-CIV$_2$ revealed a mitochondrial carrier dimer (COXMC1–2) adjacent to COX1 (Fig. 5, E and H) and a monomeric mitochondrial carrier (COXMC3) adjacent to COX3 (Fig. 5, E and I, and supplementary text).

Although both COXMC1 and COXMC2 are annotated as 2-oxoglutarate carriers (SLC25A11), key dicarboxylate-contacting residues (57) are fully conserved only for COXMC2 (Fig. 5H). The COXMC1–2 dimer is attached to the rest of Tt-CIV$_2$ via interactions with COX1's N-terminal helical extension as well as with subunit COX7C (fig. S21A). COXMC1's interactions with COX7C and COXTT22 block the accessibility from the IMS (fig. S21A), making it unlikely that COXMC1 functions as a transporter. Instead, COXMC1 may have been coopted by Tt-CIV$_2$ as a structural or regulatory subunit. The COXMC1 N-terminal loop (residues 1–8^{COXMC2}) inserts deeply into the COXMC2 central cavity (Fig. 5H). Glu4^{COXMC1} is in close vicinity of several of COXMC2's dicarboxylate-binding residues (Fig. 5H). Given the similar chemical structures of oxaloacetate and glutamate, Glu4^{COXMC1} may act as a substrate analog, placing COXMC2 in an inhibited state.

The monomeric mitochondrial carrier subunit, COXMC3, has long amphipathic α-helical extensions on both termini (Fig. 5I). These extensions interact with core subunit COX3 via bridging lipids in the IMS (fig. S21B). The N-terminal helix of COX3 also interacts with COXMC3 in the matrix (Fig. 5I). These interactions, as well as the broken symmetry of the carrier's TMHs (55) (Fig. 5I), make COXMC3 unlikely to function as a solute carrier. Rather, given its interactions on either side of the membrane and its peripheral location (fig. S21C), it is likely that COXMC3 has been coopted to help bend the *T. thermophila*'s cristae.

Tt-CIV$_2$ also contains a hexameric α-propeller domain composed of small TIM8-like subunits next to the cyt *c* crater (Fig. 5, F and J). Soluble TIM9$_3$-TIM10$_3$ (58) or TIM8$_3$-TIM13$_3$ (59) hexamers function as IMS chaperones during mitochondrial protein import (fig. S22). Moreover, a TIM9$_3$-TIM10$_2$-TIM12 hexamer forms part of the TIM22 complex (60) that inserts mitochondrial carriers into the IMM (fig. S22). In contrast to canonical soluble TIM hexamers, the Tt-CIV$_2$ TIM assembly is a hetero-hexamer of six distinct subunits (COXTIM1–6) (Fig. 5J). The TIM hexamer is anchored to Tt-CIV$_2$ via interaction with a Tt-specific loop of COX2. As seen in structures of TIM hexamers binding to substrate peptides (61), this Tt-COX2 loop embeds itself in the interhelical clefts of the COXTIM subunits (Fig. 5J). Additionally, a short Tt-COX2 helix inserts itself into the central channel of the Tt-TIM hexamer, parallel to the hexamer's pseudosymmetry axis (Fig. 5J). Human TIM8a has been implicated in CIV maturation through interactions with COX6B and assembly factors COX17 and COX19, which deliver essential copper atoms to COX2 (62). In *T. thermophila*, a group of subunits, including homologs of COX6B and COX17, are found adjacent to the TIM hexamer of Tt-CIV$_2$ (fig. S19A). These subunits may be a part of Tt-CIV's maturation pathway that stay bound to the final complex, suggesting that one pathway to subunit addition into mETC complexes may be via the permanent incorporation of assembly factors.

Conclusions

The structures of Tt-SC I+III$_2$ and Tt-CV$_2$ reveal the diversity present in eukaryotic core metabolism. Collecting cryoEM data on a partially purified sample allowed for the simultaneous structure determination of an entire metabolic pathway. This work demonstrates that ciliate mETC complexes have diverged from those of opisthokonts and

archaeplastidans, including incorporating additional accessory subunits, flipping surface charges, splitting core subunits, and enhancing inter-complex interactions to produce highly curved and symmetry-broken assemblies. Furthermore, functional differences in the *T. thermophila* mETC complexes such as the lack of a deactive state in Tt-CI allow for the disambiguation of previous observations and will contribute to a more complete understanding of the conserved mechanisms of these essential complexes.

Supplementary Material

Refer to Web version on PubMed Central for supplementary material.

ACKNOWLEDGMENTS

Data and materials availability:

Single particle cryogenic electron micrograph movies and motion corrected micrographs for Dataset 1 and Dataset 2 are available on the Electron Microscopy Public Image Archive, accession codes: EMPIAR-10882 and EMPIAR-10919. The maps and models for Tt-SC I+III$_2$ and Tt-CIV2 are available on the Electron Microscopy Database (EMDB) and the Protein Data Bank (PDB) with accession codes: Tt-SC I+III$_2$ EMDB-25882, PDB-7TGH; Tt-CIV$_2$ EMDB-32325, PDB-7W5Z. The maps for Tt-CV$_2$ are available on the EMDB with accession codes EMDB-32631 and EMDB-32632.

REFERENCES AND NOTES

1. Mitchell P, Chemiosmotic coupling in energy transduction: A logical development of biochemical knowledge. J. Bioenerg. 3, 5–24 (1972). doi:10.1007/BF01515993 [PubMed: 4263930]

2. Davies KM, Blum TB, Kühlbrandt W, Conserved in situ arrangement of complex I and III$_2$ in mitochondrial respiratory chain supercomplexes of mammals, yeast, and plants. Proc. Natl. Acad. Sci. U.S.A. 115, 3024–3029 (2018). doi:10.1073/pnas.1720702115 [PubMed: 29519876]

3. Letts JA, Sazanov LA, Clarifying the supercomplex: The higher-order organization of the mitochondrial electron transport chain. Nat. Struct. Mol. Biol. 24, 800–808 (2017). doi:10.1038/nsmb.3460 [PubMed: 28981073]

4. Shinzawa-Itoh K, Hatanaka M, Fujita K, Yano N, Ogasawara Y, Iwata J, Yamashita E, Tsukihara T, Yoshikawa S, Muramoto K, The 1.3-Å resolution structure of bovine cytochrome c oxidase suggests a dimerization mechanism. BBA Adv. 1, 100009 (2021). doi:10.1016/j.bbadva.2021.100009

5. Spikes TE, Montgomery MG, Walker JE, Structure of the dimeric ATP synthase from bovine mitochondria. Proc. Natl. Acad. Sci. U.S.A. 117, 23519–23526 (2020). doi:10.1073/pnas.2013998117 [PubMed: 32900941]

6. Davies KM, Anselmi C, Wittig I, Faraldo-Gómez JD, Kühlbrandt W, Structure of the yeast F1Fo-ATP synthase dimer and its role in shaping the mitochondrial cristae. Proc. Natl. Acad. Sci. U.S.A. 109, 13602–13607 (2012). doi:10.1073/pnas.1204593109 [PubMed: 22864911]

7. Mühleip AW, Joos F, Wigge C, Frangakis AS, Kühlbrandt W, Davies KM, Helical arrays of U-shaped ATP synthase dimers form tubular cristae in ciliate mitochondria. Proc. Natl. Acad. Sci. U.S.A. 113, 8442–8447 (2016). doi:10.1073/pnas.1525430113 [PubMed: 27402755]

8. Mühleip A, Kock Flygaard R, Ovciarikova J, Lacombe A, Fernandes P, Sheiner L, Amunts A, ATP synthase hexamer assemblies shape cristae of Toxoplasma mitochondria. Nat. Commun. 12, 120 (2021). doi:10.1038/s41467-020-20381-z [PubMed: 33402698]

9. Flygaard RK, Mühleip A, Tobiasson V, Amunts A, Type III ATP synthase is a symmetry-deviated dimer that induces membrane curvature through tetramerization. Nat. Commun. 11, 5342 (2020). doi:10.1038/s41467-020-18993-6 [PubMed: 33093501]

10. Stroud DA, Surgenor EE, Formosa LE, Reljic B, Frazier AE, Dibley MG, Osellame LD, Stait T, Beilharz TH, Thorburn DR, Salim A, Ryan MT, Accessory subunits are integral for assembly and function of human mitochondrial complex I. Nature 538, 123–126 (2016). doi:10.1038/nature19754 [PubMed: 27626371]

11. Padavannil A, Ayala-Hernandez MG, Castellanos-Silva EA, Letts JA, The Mysterious Multitude: Structural Perspective on the Accessory Subunits of Respiratory Complex I. Front. Mol. Biosci. 8, 798353 (2022). doi:10.3389/fmolb.2021.798353 [PubMed: 35047558]

12. Parey K, Haapanen O, Sharma V, Köfeler H, Züllig T, Prinz S, Siegmund K, Wittig I, Mills DJ, Vonck J, Kühlbrandt W, Zickermann V, High-resolution cryo-EM structures of respiratory complex I: Mechanism, assembly, and disease. Sci. Adv. 5, eaax9484 (2019). doi:10.1126/sciadv.aax9484 [PubMed: 31844670]

13. Kampjut D, Sazanov LA, The coupling mechanism of mammalian respiratory complex I. Science 370, eabc4209–18 (2020). doi:10.1126/science.abc4209 [PubMed: 32972993]

14. Maldonado M, Padavannil A, Zhou L, Guo F, Letts JA, Atomic structure of a mitochondrial complex I intermediate from vascular plants. eLife 9, e56664 (2020). doi:10.7554/eLife.56664 [PubMed: 32840211]

15. Klusch N, Senkler J, Yildiz Ö, Kühlbrandt W, Braun H-P, A ferredoxin bridge connects the two arms of plant mitochondrial complex I. Plant Cell 33, 2072 (2021). doi:10.1093/plcell/koab092 [PubMed: 33768254]

16. Soufari H, Parrot C, Kuhn L, Waltz F, Hashem Y, Specific features and assembly of the plant mitochondrial complex I revealed by cryo-EM. Nat. Commun. 11, 5195 (2020). doi:10.1038/s41467-020-18814-w [PubMed: 33060577]

17. Elurbe DM, Huynen MA, The origin of the supernumerary subunits and assembly factors of complex I: A treasure trove of pathway evolution. Biochim. Biophys. Acta 1857, 971–979 (2016). doi:10.1016/j.bbabio.2016.03.027 [PubMed: 27048931]

18. Hartley AM, Lukoyanova N, Zhang Y, Cabrera-Orefice A, Arnold S, Meunier B, Pinotsis N, Maréchal A, Structure of yeast cytochrome c oxidase in a supercomplex with cytochrome bc$_1$. Nat. Struct. Mol. Biol. 26, 78–83 (2019). [PubMed: 30598554]

19. Xia D, Yu C-A, Kim H, Xia J-Z, Kachurin AM, Zhang L, Yu L, Deisenhofer J, Crystal structure of the cytochrome bc1 complex from bovine heart mitochondria. Science 277, 60–66 (1997). doi:10.1126/science.277.5322.60 [PubMed: 9204897]

20. Maldonado M, Guo F, Letts JA, Atomic structures of respiratory complex III$_2$, complex IV, and supercomplex III$_2$-IV from vascular plants. eLife 10, e62047 (2021). doi:10.7554/eLife.62047 [PubMed: 33463523]

21. Srivastava AP, Luo M, Zhou W, Symersky J, Bai D, Chambers MG, Faraldo-Gómez JD, Liao M, Mueller DM, High-resolution cryo-EM analysis of the yeast ATP synthase in a lipid membrane. Science 360, eaas9699 (2018). doi:10.1126/science.aas9699 [PubMed: 29650704]

22. Allegretti M, Klusch N, Mills DJ, Vonck J, Kühlbrandt W, Davies KM, Horizontal membrane-intrinsic α-helices in the stator a-subunit of an F-type ATP synthase. Nature 521, 237–240 (2015). doi:10.1038/nature14185 [PubMed: 25707805]

23. Gahura O, Mühleip A, Hierro-Yap C, Panicucci B, Jain M, Hollaus D, Slapni ková M, Amunts A, Zíková A, An ancestral interaction module promotes oligomerization in divergent mitochondrial ATP synthases. bioRxiv 463820 (2021). doi:10.1101/2021.10.10.463820

24. Mühleip A, McComas SE, Amunts A, Structure of a mitochondrial ATP synthase with bound native cardiolipin. eLife 8, e51179 (2019). doi:10.7554/eLife.51179 [PubMed: 31738165]

25. Blum TB, Hahn A, Meier T, Davies KM, Kühlbrandt W, Dimers of mitochondrial ATP synthase induce membrane curvature and self-assemble into rows. Proc. Natl. Acad. Sci. U.S.A. 116, 4250–4255 (2019). doi:10.1073/pnas.1816556116 [PubMed: 30760595]

26. Eichel HJ, Respiratory enzyme studies in tetrahymena pyriformis. II. Reduced diphosphopyridine nucleotide oxidase and reduced diphosphopyridine nucleotide cytochrome c reductase. J. Biol. Chem. 222, 121–136 (1956). doi:10.1016/S0021-9258(19)50777-3 [PubMed: 13366985]

27. Brunk CF, Lee LC, Tran AB, Li J, Complete sequence of the mitochondrial genome of Tetrahymena thermophila and comparative methods for identifying highly divergent genes. Nucleic Acids Res. 31, 1673–1682 (2003). doi:10.1093/nar/gkg270 [PubMed: 12626709]

28. Kilpatrick L, Ereci ska M, Mitochondrial respiratory chain of Tetrahymena pyriformis: The properties of submitochondrial particles and the soluble b and c type pigments. Biochim. Biophys. Acta 462, 515–530 (1977). doi:10.1016/0005-2728(77)90098-6 [PubMed: 202305]

29. Smith DGS, Gawryluk RMR, Spencer DF, Pearlman RE, Siu KWM, Gray MW, Exploring the mitochondrial proteome of the ciliate protozoon Tetrahymena thermophila: Direct analysis by tandem mass spectrometry. J. Mol. Biol. 374, 837–863 (2007). doi:10.1016/j.jmb.2007.09.051 [PubMed: 17959197]

30. Maclean AE, Bridges HR, Silva MF, Ding S, Ovciarikova J, Hirst J, Sheiner L, Complexome profile of Toxoplasma gondii mitochondria identifies divergent subunits of respiratory chain complexes including new subunits of cytochrome bc1 complex. PLOS Pathog. 17, e1009301 (2021). doi:10.1371/journal.ppat.1009301 [PubMed: 33651838]

31. Evers F, Cabrera-Orefice A, Elurbe DM, Kea-Te Lindert M, Boltryk SD, Voss TS, Huynen MA, Brandt U, Kooij TWA, Composition and stage dynamics of mitochondrial complexes in Plasmodium falciparum. Nat. Commun. 12, 3820 (2021). doi:10.1038/s41467-021-23919-x [PubMed: 34155201]

32. Londer YY, Expression of recombinant cytochromes c in E. coli. Methods Mol. Biol. 705, 123–150 (2011). doi:10.1007/978-1-61737-967-3_8 [PubMed: 21125384]

33. Ho C-M, Li X, Lai M, Terwilliger TC, Beck JR, Wohlschlegel J, Goldberg DE, Fitzpatrick AWP, Zhou ZH, Bottom-up structural proteomics: cryoEM of protein complexes enriched from the cellular milieu. Nat. Methods 17, 79–85 (2020). [PubMed: 31768063]

34. Letts JA, Fiedorczuk K, Degliesposti G, Skehel M, Sazanov LA, Structures of Respiratory Supercomplex I+III$_2$ Reveal Functional and Conformational Crosstalk. Mol. Cell 75, 1131–1146.e6 (2019). doi:10.1016/j.molcel.2019.07.022 [PubMed: 31492636]

35. Zong S, Wu M, Gu J, Liu T, Guo R, Yang M, Structure of the intact 14-subunit human cytochrome c oxidase. Cell Res. 28, 1026–1034 (2018). doi:10.1038/s41422-018-0071-1 [PubMed: 30030519]

36. Agip AA, Blaza JN, Bridges HR, Viscomi C, Rawson S, Muench SP, Hirst J, Cryo-EM structures of complex I from mouse heart mitochondria in two biochemically defined states. Nat. Struct. Mol. Biol. 25, 548–556 (2018). doi:10.1038/s41594-018-0073-1 [PubMed: 29915388]

37. Parey K, Brandt U, Xie H, Mills DJ, Siegmund K, Vonck J, Kühlbrandt W, Zickermann V, Cryo-EM structure of respiratory complex I at work. eLife 7, e39213 (2018). doi:10.7554/eLife.39213 [PubMed: 30277212]

38. Parey K, Lasham J, Mills DJ, Djurabekova A, Haapanen O, Yoga EG, Xie H, Kühlbrandt W, Sharma V, Vonck J, Zickermann V, High-resolution structure and dynamics of mitochondrial complex I—Insights into the proton pumping mechanism. Sci. Adv. 7, eabj3221 (2021). doi:10.1126/sciadv.abj3221 [PubMed: 34767441]

39. Maklashina E, Kotlyar AB, Cecchini G, Active/de-active transition of respiratory complex I in bacteria, fungi, and animals. Biochim. Biophys. Acta 1606, 95–103 (2003). doi:10.1016/S0005-2728(03)00087-2 [PubMed: 14507430]

40. Blaza JN, Vinothkumar KR, Hirst J, Structure of the Deactive State of Mammalian Respiratory Complex I. Structure 26, 312–319.e3 (2018). doi:10.1016/j.str.2017.12.014 [PubMed: 29395787]

41. Gavrikova EV, Vinogradov AD, Active/de-active state transition of the mitochondrial complex I as revealed by specific sulfhydryl group labeling. FEBS Lett. 455, 36–40 (1999). doi:10.1016/S0014-5793(99)00850-9 [PubMed: 10428467]

42. Cabrera-Orefice A, Yoga EG, Wirth C, Siegmund K, Zwicker K, Guerrero-Castillo S, Zickermann V, Hunte C, Brandt U, Locking loop movement in the ubiquinone pocket of complex I disengages the proton pumps. Nat. Commun. 9, 4500 (2018). doi:10.1038/s41467-018-06955-y [PubMed: 30374105]

43. Sousa JS, Mills DJ, Vonck J, Kühlbrandt W, Functional asymmetry and electron flow in the bovine respirasome. eLife 5, e21290 (2016). doi:10.7554/eLife.21290 [PubMed: 27830641]

44. Vercellino I, Sazanov LA, Structure and assembly of the mammalian mitochondrial supercomplex CIII2CIV. Nature 598, 364–367 (2021). doi:10.1038/s41586-021-03927-z [PubMed: 34616041]

45. Xia D, Esser L, Tang W-K, Zhou F, Zhou Y, Yu L, Yu C-A, Structural analysis of cytochrome bc1 complexes: Implications to the mechanism of function. Biochim. Biophys. Acta 1827, 1278–1294 (2013). doi:10.1016/j.bbabio.2012.11.008 [PubMed: 23201476]

46. Iwata S, Lee JW, Okada K, Lee JK, Iwata M, Rasmussen B, Link TA, Ramaswamy S, Jap BK, Complete structure of the 11-subunit bovine mitochondrial cytochrome bc1 complex. Science 281, 64–71 (1998). doi:10.1126/science.281.5373.64 [PubMed: 9651245]

47. Malone LA, Qian P, Mayneord GE, Hitchcock A, Farmer DA, Thompson RF, Swainsbury DJK, Ranson NA, Hunter CN, Johnson MP, Cryo-EM structure of the spinach cytochrome b6 f complex at 3.6 Å resolution. Nature 575, 535–539 (2019). doi:10.1038/s41586-019-1746-6 [PubMed: 31723268]

48. wierczek M, Cieluch E, Sarewicz M, Borek A, Moser CC, Dutton PL, Osyczka A, An electronic bus bar lies in the core of cytochrome bc1. Science 329, 451–454 (2010). doi:10.1126/science.1190899 [PubMed: 20651150]

49. Cramer WA, Hasan SS, Yamashita E, The Q cycle of cytochrome bc complexes: A structure perspective. Biochim. Biophys. Acta Bioenerg. 1807, 788–802 (2011). doi:10.1016/j.bbabio.2011.02.006

50. Brzezinski P, Moe A, Ädelroth P, Structure and Mechanism of Respiratory III-IV Supercomplexes in Bioenergetic Membranes. Chem. Rev. 121, 9644–9673 (2021). doi:10.1021/acs.chemrev.1c00140 [PubMed: 34184881]

51. Rich PR, Maréchal A, Functions of the hydrophilic channels in protonmotive cytochrome c oxidase. J. R. Soc. Interface 10, 20130183 (2013). doi:10.1098/rsif.2013.0183 [PubMed: 23864498]

52. Maréchal A, Xu J-Y, Genko N, Hartley AM, Haraux F, Meunier B, Rich PR, A common coupling mechanism for A-type heme-copper oxidases from bacteria to mitochondria. Proc. Natl. Acad. Sci. U.S.A. 117, 9349–9355 (2020). doi:10.1073/pnas.2001572117 [PubMed: 32291342]

53. Yoshikawa S, Muramoto K, Shinzawa-Itoh K, The O_2 reduction and proton pumping gate mechanism of bovine heart cytochrome c oxidase. Biochim. Biophys. Acta 1807, 1279–1286 (2011). doi:10.1016/j.bbabio.2011.06.008 [PubMed: 21718684]

54. Koepke J, Olkhova E, Angerer H, Müller H, Peng G, Michel H, High resolution crystal structure of Paracoccus denitrificans cytochrome c oxidase: New insights into the active site and the proton transfer pathways. Biochim. Biophys. Acta Bioenerg. 1787, 635–645 (2009). doi:10.1016/j.bbabio.2009.04.003

55. Ruprecht JJ, Kunji ERS, Structural Mechanism of Transport of Mitochondrial Carriers. Annu. Rev. Biochem. 90, 535–558 (2021). doi:10.1146/annurev-biochem-072820-020508 [PubMed: 33556281]

56. Lu Y-W, Acoba MG, Selvaraju K, Huang T-C, Nirujogi RS, Sathe G, Pandey A, Claypool SM, Human adenine nucleotide translocases physically and functionally interact with respirasomes. Mol. Biol. Cell 28, 1489–1506 (2017). doi:10.1091/mbc.e17-03-0195 [PubMed: 28404750]

57. Monné M, Miniero DV, Iacobazzi V, Bisaccia F, Fiermonte G, The mitochondrial oxoglutarate carrier: From identification to mechanism. J. Bioenerg. Biomembr. 45, 1–13 (2013). doi:10.1007/s10863-012-9475-7 [PubMed: 23054077]

58. Webb CT, Gorman MA, Lazarou M, Ryan MT, Gulbis JM, Crystal structure of the mitochondrial chaperone TIM9.10 reveals a six-bladed alpha-propeller. Mol. Cell 21, 123–133 (2006). doi:10.1016/j.molcel.2005.11.010 [PubMed: 16387659]

59. Baker MJ, Webb CT, Stroud DA, Palmer CS, Frazier AE, Guiard B, Chacinska A, Gulbis JM, Ryan MT, Structural and functional requirements for activity of the Tim9-Tim10 complex in mitochondrial protein import. Mol. Biol. Cell 20, 769–779 (2009). doi:10.1091/mbc.e08-09-0903 [PubMed: 19037098]

60. Wiedemann N, Pfanner N, Mitochondrial Machineries for Protein Import and Assembly. Annu. Rev. Biochem. 86, 685–714 (2017). doi:10.1146/annurev-biochem-060815-014352 [PubMed: 28301740]

61. Weinhäupl K, Lindau C, Hessel A, Wang Y, Schütze C, Jores T, Melchionda L, Schönfisch B, Kalbacher H, Bersch B, Rapaport D, Brennich M, Lindorff-Larsen K, Wiedemann N, Schanda P, Structural Basis of Membrane Protein Chaperoning through the Mitochondrial Intermembrane Space. Cell 175, 1365–1379.e25 (2018). doi:10.1016/j.cell.2018.10.039 [PubMed: 30445040]

62. Ghosh A, Pratt AT, Soma S, Theriault SG, Griffin AT, Trivedi PP, Gohil VM, Mitochondrial disease genes COA6, COX6B and SCO2 have overlapping roles in COX2 biogenesis. Hum. Mol. Genet. 25, 660–671 (2016). doi:10.1093/hmg/ddv503 [PubMed: 26669719]

63. Kurisu G, Zhang H, Smith JL, Cramer WA, Structure of the cytochrome b6f complex of oxygenic photosynthesis: Tuning the cavity. Science 302, 1009–1014 (2003). doi:10.1126/science.1090165 [PubMed: 14526088]

64. Kleinschroth T, Castellani M, Trinh CH, Morgner N, Brutschy B, Ludwig B, Hunte C, X-ray structure of the dimeric cytochrome bc1 complex from the soil bacterium Paracoccus denitrificans at 2.7-Å resolution. Biochim. Biophys. Acta Bioenerg. 1807, 1606–1615 (2011). doi:10.1016/j.bbabio.2011.09.017

65. Gutiérrez JC, Orias E, Genetic characterization of Tetrahymena thermophila mutants unable to secrete capsules. Dev. Genet. 13, 160–166 (1992). doi:10.1002/dvg.1020130210 [PubMed: 1499157]

66. Balabaskaran Nina P, Dudkina NV, Kane LA, van Eyk JE, Boekema EJ, Mather MW, Vaidya AB, Highly divergent mitochondrial ATP synthase complexes in Tetrahymena thermophila. PLOS Biol. 8, e1000418–e15 (2010). doi:10.1371/journal.pbio.1000418 [PubMed: 20644710]

67. Schertl P, Braun H-P, Activity measurements of mitochondrial enzymes in native gels. Methods Mol. Biol. 1305, 131–138 (2015). doi:10.1007/978-1-4939-2639-8_9 [PubMed: 25910731]

68. Arslan E, Schulz H, Zufferey R, Künzler P, Thöny-Meyer L, Overproduction of the Bradyrhizobium japonicum c-type cytochrome subunits of the cbb3 oxidase in Escherichia coli. Biochem. Biophys. Res. Commun. 251, 744–747 (1998). doi:10.1006/bbrc.1998.9549 [PubMed: 9790980]

69. Zheng SQ, Palovcak E, Armache J-P, Verba KA, Cheng Y, Agard DA, MotionCor2: Anisotropic correction of beam-induced motion for improved cryo-electron microscopy. Nat. Methods 14, 331–332 (2017). doi:10.1038/nmeth.4193 [PubMed: 28250466]

70. Rohou A, Grigorieff N, CTFFIND4: Fast and accurate defocus estimation from electron micrographs. J. Struct. Biol. 192, 216–221 (2015). doi:10.1016/j.jsb.2015.08.008 [PubMed: 26278980]

71. Zivanov J, Nakane T, Forsberg BO, Kimanius D, Hagen WJ, Lindahl E, Scheres SHW, New tools for automated high-resolution cryo-EM structure determination in RELION-3. eLife 7, e42166 (2018). doi:10.7554/eLife.42166 [PubMed: 30412051]

72. Wagner T, Merino F, Stabrin M, Moriya T, Gatsogiannis C, Raunser S, SPHIRE-crYOLO is a fast and accurate fully automated particle picker for cryo-EM. Commun. Biol. 2, 218 (2019). doi:10.1038/s42003-019-0437-z [PubMed: 31240256]

73. Punjani A, Rubinstein JL, Fleet DJ, Brubaker MA, cryoSPARC: Algorithms for rapid unsupervised cryo-EM structure determination. Nat. Methods 14, 290–296 (2017). doi:10.1038/nmeth.4169 [PubMed: 28165473]

74. Punjani A, Zhang H, Fleet DJ, Non-uniform refinement: Adaptive regularization improves single-particle cryo-EM reconstruction. Nat. Methods 17, 1214–1221 (2020). doi:10.1038/s41592-020-00990-8 [PubMed: 33257830]

75. Zivanov J, Nakane T, Scheres SHW, A Bayesian approach to beam-induced motion correction in cryo-EM single-particle analysis. IUCrJ 6, 5–17 (2019). doi:10.1107/S205225251801463X

76. Hart D, Cianfrocco MA, Wong-Barnum M, Youn C, Wagner R, Leschziner A, COSMIC2: A Science Gateway for Cryo-Electron Microscopy Structure Determination. In PEARC17: Practice and Experience in Advanced Research Computing (2017). doi:10.1145/3093338.3093390

77. Sanchez-Garcia R, Gomez-Blanco J, Cuervo A, Carazo JM, Sorzano COS, Vargas J, DeepEMhancer: A deep learning solution for cryo-EM volume post-processing. Commun. Biol. 4, 874 (2021). doi:10.1038/s42003-021-02399-1 [PubMed: 34267316]

78. Liebschner D, Afonine PV, Baker ML, Bunkóczi G, Chen VB, Croll TI, Hintze B, Hung L-W, Jain S, McCoy AJ, Moriarty NW, Oeffner RD, Poon BK, Prisant MG, Read RJ, Richardson JS, Richardson DC, Sammito MD, Sobolev OV, Stockwell DH, Terwilliger TC, Urzhumtsev AG, Videau LL, Williams CJ, Adams PD, Macromolecular structure determination using X-rays, neutrons and electrons: Recent developments in Phenix. Acta Crystallogr. D 75, 861–877 (2019). doi:10.1107/S2059798319011471

79. Morin A, Eisenbraun B, Key J, Sanschagrin PC, Timony MA, Ottaviano M, Sliz P, Collaboration gets the most out of software. eLife 2, e01456 (2013). doi:10.7554/eLife.01456 [PubMed: 24040512]

80. Emsley P, Lohkamp B, Scott WG, Cowtan K, Features and development of Coot. Acta Crystallogr. D 66, 486–501 (2010). doi:10.1107/S0907444910007493 [PubMed: 20383002]

81. Kelley LA, Mezulis S, Yates CM, Wass MN, Sternberg MJE, The Phyre2 web portal for protein modeling, prediction and analysis. Nat. Protoc. 10, 845–858 (2015). doi:10.1038/nprot.2015.053 [PubMed: 25950237]

82. Goyal A, Verma P, Anandhakrishnan M, Gokhale RS, Sankaranarayanan R, Molecular basis of the functional divergence of fatty acyl-AMP ligase biosynthetic enzymes of Mycobacterium tuberculosis. J. Mol. Biol. 416, 221–238 (2012). doi:10.1016/j.jmb.2011.12.031 [PubMed: 22206988]

83. Gakh O, Cavadini P, Isaya G, Mitochondrial processing peptidases. Biochim. Biophys. Acta Mol. Cell Res. 1592, 63–77 (2002). doi:10.1016/S0167-4889(02)00265-3

84. Gao X, Wen X, Esser L, Quinn B, Yu L, Yu C-A, Xia D, Structural basis for the quinone reduction in the bc1 complex: A comparative analysis of crystal structures of mitochondrial cytochrome bc1 with bound substrate and inhibitors at the Qi site. Biochemistry 42, 9067–9080 (2003). doi:10.1021/bi0341814 [PubMed: 12885240]

85. Esser L, Quinn B, Li Y-F, Zhang M, Elberry M, Yu L, Yu C-A, Xia D, Crystallographic studies of quinol oxidation site inhibitors: A modified classification of inhibitors for the cytochrome bc_1 complex. J. Mol. Biol. 341, 281–302 (2004). doi:10.1016/j.jmb.2004.05.065 [PubMed: 15312779]

86. Walsh P, Bursa D, Law YC, Cyr D, Lithgow T, The J-protein family: Modulating protein assembly, disassembly and translocation. EMBO Rep. 5, 567–571 (2004). doi:10.1038/sj.embor.7400172 [PubMed: 15170475]

87. Andrews B, Carroll J, Ding S, Fearnley IM, Walker JE, Assembly factors for the membrane arm of human complex I. Proc. Natl. Acad. Sci. U.S.A. 110, 18934–18939 (2013). doi:10.1073/pnas.1319247110 [PubMed: 24191001]

88. Riistama S, Puustinen A, García-Horsman A, Iwata S, Michel H, Wikström M, Channelling of dioxygen into the respiratory enzyme. Biochim. Biophys. Acta Bioenerg. 1275, 1–4 (1996). doi:10.1016/0005-2728(96)00040-0

89. Hannibal L, Tomasina F, Capdevila DA, Demicheli V, Tórtora V, Alvarez-Paggi D, Jemmerson R, Murgida DH, Radi R, Alternative Conformations of Cytochrome c: Structure, Function, and Detection. Biochemistry 55, 407–428 (2016). doi:10.1021/acs.biochem.5b01385 [PubMed: 26720007]

90. Berghuis AM, Guillemette JG, Smith M, Brayer GD, Mutation of tyrosine-67 to phenylalanine in cytochrome c significantly alters the local heme environment. J. Mol. Biol. 235, 1326–1341 (1994). doi:10.1006/jmbi.1994.1086 [PubMed: 8308895]

91. Alvarez-Paggi D, Castro MA, Tórtora V, Castro L, Radi R, Murgida DH, Electrostatically driven second-sphere ligand switch between high and low reorganization energy forms of native

cytochrome c. J. Am. Chem. Soc. 135, 4389–4397 (2013). doi:10.1021/ja311786b [PubMed: 23458571]

92. Koyama M, Sasaki T, Sasaki N, Matsuura Y, Crystal structure of human WBSCR16, an RCC1-like protein in mitochondria. Protein Sci. 26, 1870–1877 (2017). doi:10.1002/pro.3210 [PubMed: 28608466]

93. Reyes A, Favia P, Vidoni S, Petruzzella V, Zeviani M, RCC1L (WBSCR16) isoforms coordinate mitochondrial ribosome assembly through their interaction with GTPases. PLOS Genet. 16, e1008923 (2020). doi:10.1371/journal.pgen.1008923 [PubMed: 32735630]

94. Huang G, Massoudi D, Muir AM, Joshi DC, Zhang C-L, Chiu SY, Greenspan DS, WBSCR16 Is a Guanine Nucleotide Exchange Factor Important for Mitochondrial Fusion. Cell Rep. 20, 923–934 (2017). doi:10.1016/j.celrep.2017.06.090 [PubMed: 28746876]

95. Vonrhein C, Bönisch H, Schäfer G, Schulz GE, The structure of a trimeric archaeal adenylate kinase. J. Mol. Biol. 282, 167–179 (1998). doi:10.1006/jmbi.1998.2003 [PubMed: 9733648]

96. Helling S, Hüttemann M, Ramzan R, Kim SH, Lee I, Müller T, Langenfeld E, Meyer HE, Kadenbach B, Vogt S, Marcus K, Multiple phosphorylations of cytochrome c oxidase and their functions. Proteomics 12, 950–959 (2012). doi:10.1002/pmic.201100618 [PubMed: 22522801]

97. Zhang Y, Fernie AR, On the Detection and Functional Significance of the Protein-Protein Interactions of Mitochondrial Transport Proteins. Biomolecules 10, 1107 (2020). doi:10.3390/biom10081107

98. Lunetti P, Damiano F, De Benedetto G, Siculella L, Pennetta A, Muto L, Paradies E, Marobbio CMT, Dolce V, Capobianco L, Characterization of Human and Yeast Mitochondrial Glycine Carriers with Implications for Heme Biosynthesis and Anemia. J. Biol. Chem. 291, 19746–19759 (2016). doi:10.1074/jbc.M116.736876 [PubMed: 27476175]

99. Ogunbona OB, Claypool SM, Emerging Roles in the Biogenesis of Cytochrome c Oxidase for Members of the Mitochondrial Carrier Family. Front. Cell Dev. Biol. 7, 3 (2019). doi:10.3389/fcell.2019.00003 [PubMed: 30766870]

100. Solmaz SRN, Hunte C, Structure of complex III with bound cytochrome c in reduced state and definition of a minimal core interface for electron transfer. J. Biol. Chem. 283, 17542–17549 (2008). doi:10.1074/jbc.M710126200 [PubMed: 18390544]

101. Shimada S, Shinzawa-Itoh K, Baba J, Aoe S, Shimada A, Yamashita E, Kang J, Tateno M, Yoshikawa S, Tsukihara T, Complex structure of cytochrome c-cytochrome c oxidase reveals a novel protein-protein interaction mode. EMBO J. 36, 291–300 (2017). doi:10.15252/embj.201695021 [PubMed: 27979921]

102. Holm L, Sander C, Dali: A network tool for protein structure comparison. Trends Biochem. Sci. 20, 478–480 (1995). doi:10.1016/S0968-0004(00)89105-7 [PubMed: 8578593]
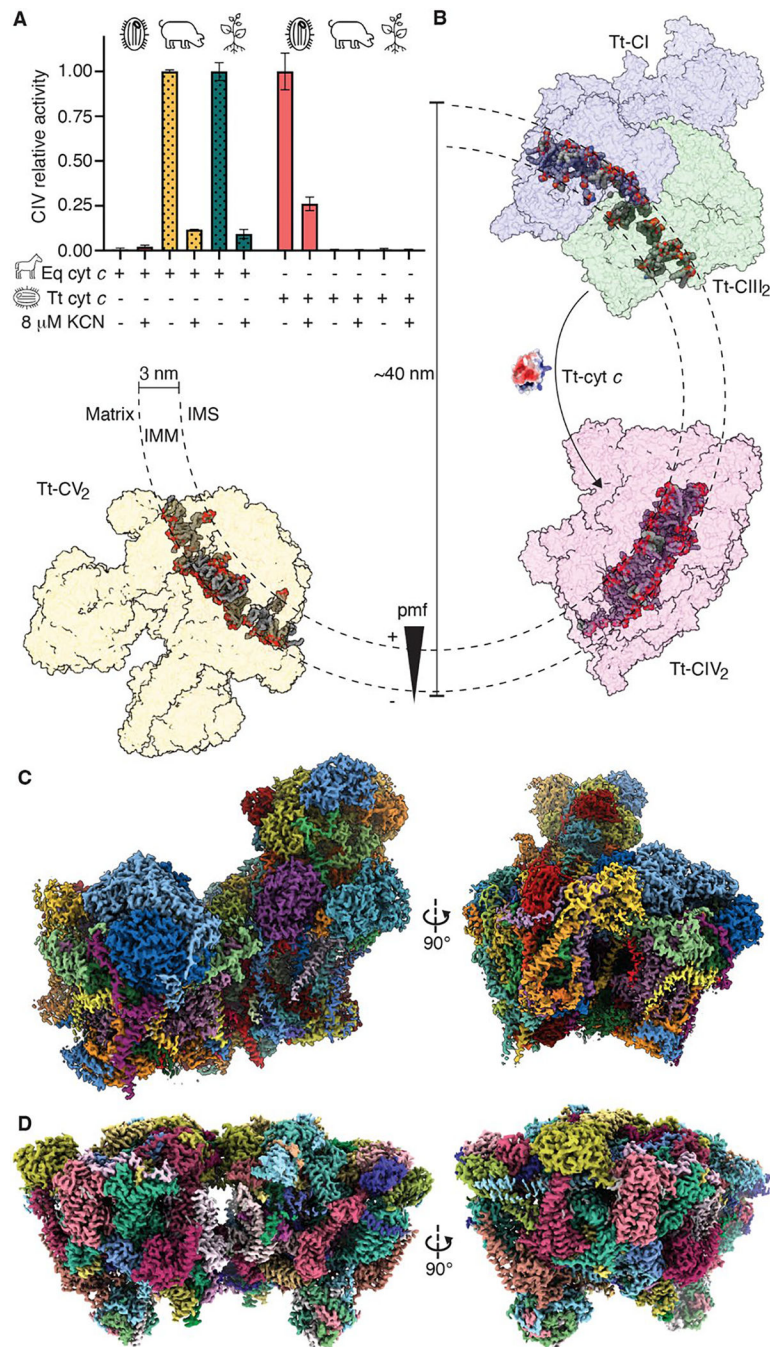
Fig. 1. Functional and structural divergence of *T. thermophila*'s electron transport chain.
(**A**) Relative CIV activity of isolated mitochondrial membranes from *T. thermophila* (ciliate symbol, red), *S. scrofa* (pig symbol, yellow) and *V. radiata* (plant symbol, green) using cyt *c* from horse (Eq, horse symbol, dotted) or *T. thermophila* (Tt, ciliate symbol, solid) in the presence or absence of 8 μM potassium cyanide (KCN). Average, SEM (n=4). (**B**) Representation of *T. thermophila*'s mitochondrial electron transport chain on a tubular crista with the width of the membrane determined by the observed phospholipids and hydrophobic regions of the complexes. Complexes shown in surface (Tt-CI, blue; Tt-CIII₂,

green; Tt-CIV$_2$, pink; Tt-CV$_2$, yellow, PDB: 6YNY (9). Lipids shown in sphere, colored by heteroatom. Cyt *c* homology model shown in surface, colored by electrostatic potential. The arrow shows approximate binding sites for cyt *c* on Tt-CIII$_2$ and TtCIV$_2$. IMS, intermembrane space; pmf, protonmotive force. (**C**) CryoEM map of Tt-SC I+III$_2$ colored by individual subunits. (**D**) CryoEM map of Tt-CIV$_2$ colored by individual subunits.
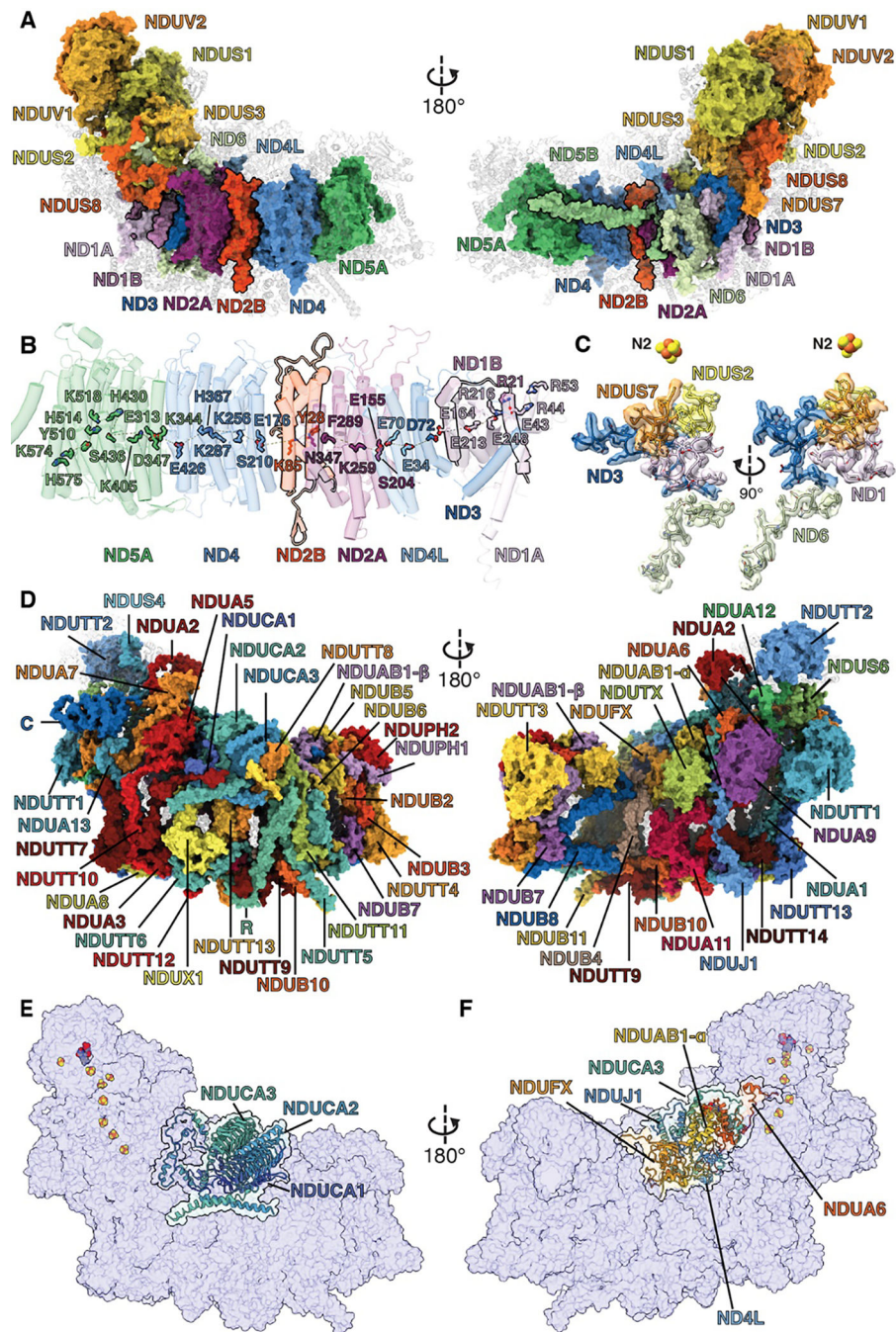
Fig. 2. Structural and functional features of Tt-CI.

(**A**) Tt-CI's 17 core subunits in colored surfaces, accessory subunits in grey cartoons. Core subunits ND1B, ND2B and ND5B highlighted with black borders. (**B**) Hydrophilic axis along the membrane arm of Tt-CI. Core subunits that form the membrane arm shown in colored cylinders, colored as in (A). Core subunits ND1B and ND2B highlighted with black borders. Conserved charged residues along the hydrophilic axis as sticks, colored by subunit. (**C**) Q-site loops shown as cartoons embedded in the density, colored by subunit. Terminal iron-sulfur cluster N2 is shown as spheres, residues shown as sticks. (**D**) The 51 accessory

subunits shown in colored surfaces, core subunits in grey transparent cartoons. (**E**) Tt-CI's three γ-carbonic anhydrase subunits in colored cartoons on Tt-CI surface (blue). (**F**) Tt-CI's ferredoxin bridge colored as cartoons on Tt-CI surface (blue).
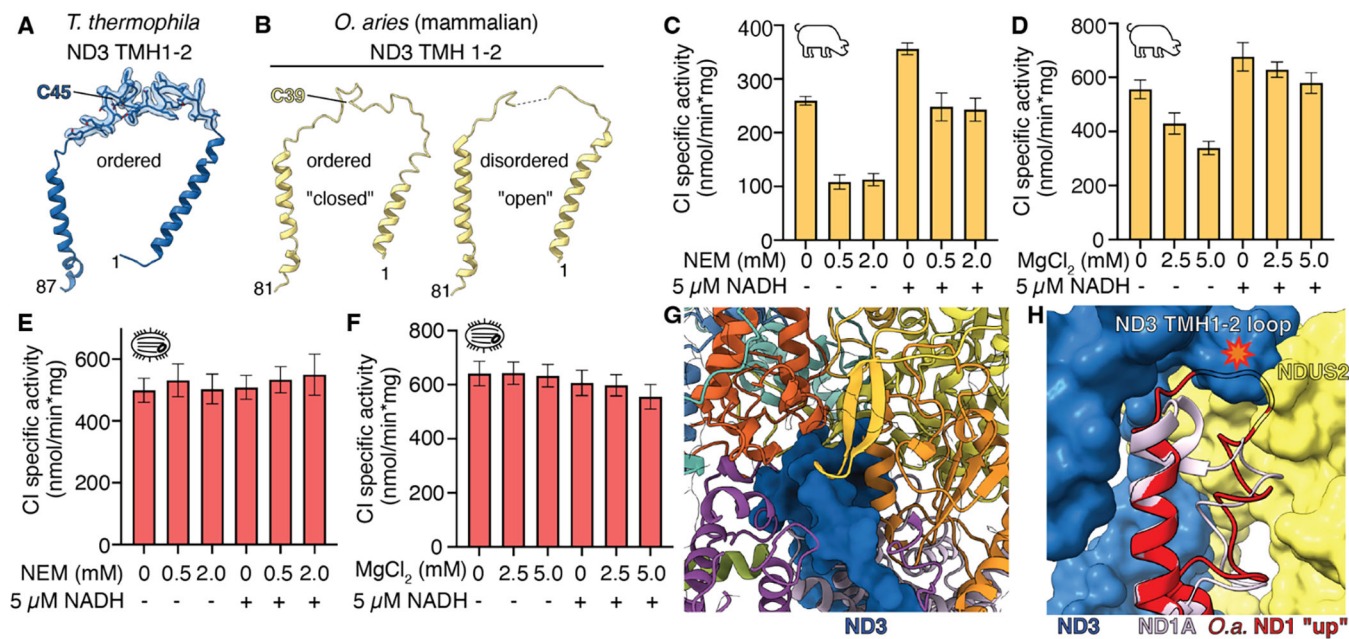
Fig. 3. Structural and functional comparison of complex I's active-to-deactive (A/D) transition.
(**A** and **B**) Comparison of complex I's ND3 TMH1–2 loop in *T. thermophila* (A) and *O. aries* (B) in the ordered ("closed", PDB: 6ZKO) and disordered ("open", PDB: 6ZKS) conformations. (**C** to **F**) Functional characterization of A/D in isolated mitochondrial membranes of *S. scrofa* (C and D) and *T. thermophila* (E and F) by spectroscopic measurement of NADH dehydrogenase activity at 340 nm in the presence of the indicated concentrations of n-ethylmaleimide (NEM) (C,E) or MgCl$_2$ (D,F) with pre-incubation with 5 μM NADH or water. Average, SEM, n=3–4. (**G**) Crowding around Tt-CI's ND3 TMH1–2 loop. ND3 in blue surface. Secondary structure elements of various accessory subunits that pack against the ND3 loop in colored cartoon. Accessory subunits colored as in Fig. 2. (**H**) Superposition of *T. thermophila* ND1 (light purple cartoon) with *O. aries* ND1 in NADH-bound, open-state CI ("up" conformation, red cartoon, PDB: 6ZKH). *O. aries* ND1 up conformation would clash with ND3 TMH1–3 loop (blue surface) and NDUFS2 (yellow surface). Clash marked with red star.
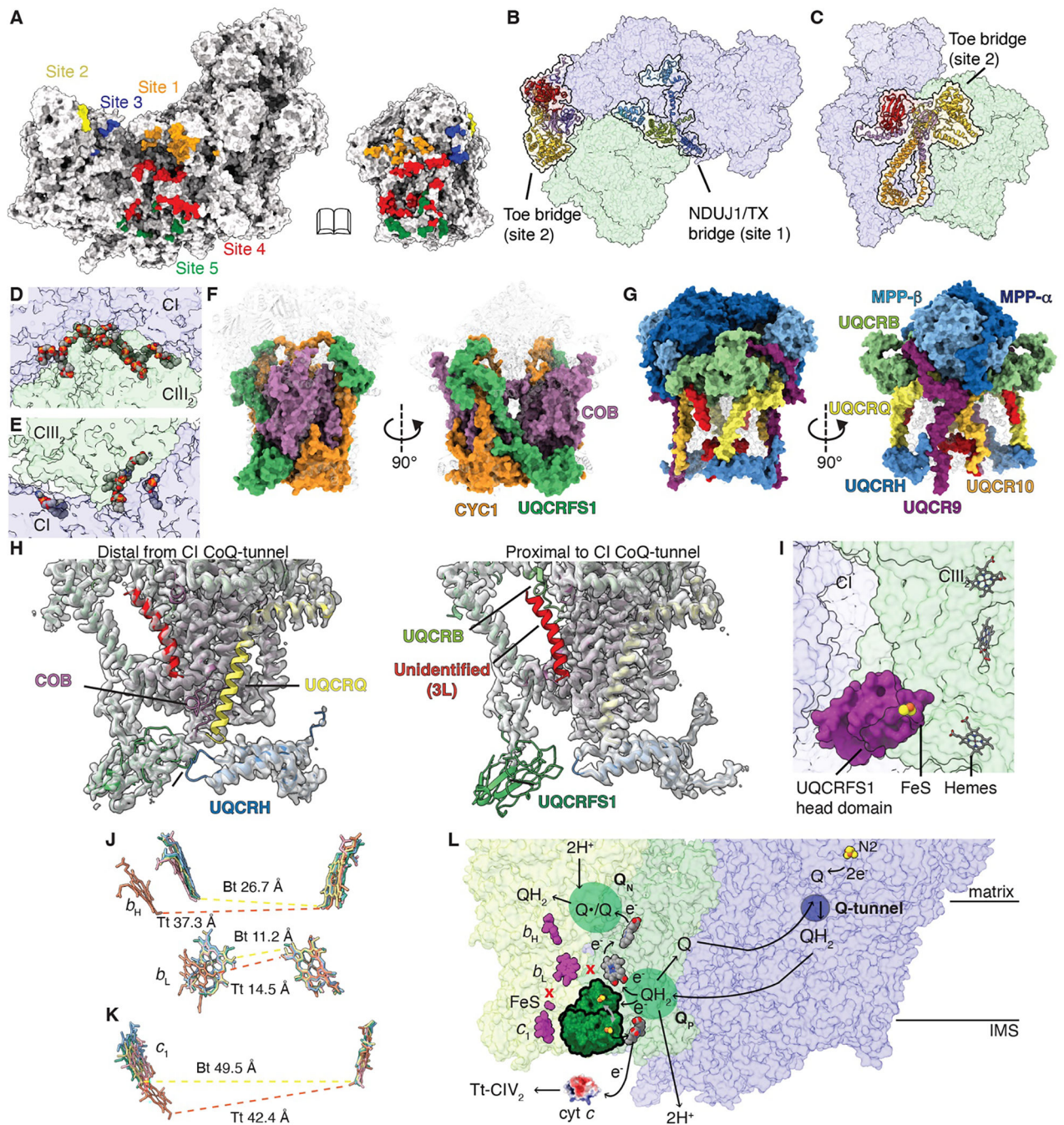
Fig. 4. (preceding page). Tt-SC I+III$_2$ interactions and Tt-CIII$_2$ symmetry breaking.
(**A**) Contact sites between Tt-CI and Tt-CIII$_2$ in Tt-SC I+III$_2$, color-coded and shown in open-book configuration. Site 1, orange; site 2, yellow; site 3, blue; site 4, red; site 5, green. (**B** and **C**) *T. thermophila*-specific Tt-SC I+III$_2$ matrix bridges (NDUJ1/TX bridge and toe bridge) in the context of Tt-SC I+III$_2$, viewed from the matrix (B) or from the plane of the membrane (C). Key subunits in colored cartoons and highlighted in black outline. (**D** and **E**) Modeled lipids (spheres) at the interface between Tt-CI (blue surface) and Tt-CIII$_2$ (green surface). Lipids at the matrix (D) or intermembrane space (E) leaflet of the membrane

viewed from the matrix or IMS, respectively. (**F** and **G**) Structure of Tt-CIII$_2$, with core (F) or accessory (G) subunits in surface and the rest of the complex in transparent cartoon. Unidentified chains (poly-ala model) in red. (**H**) Broken symmetry in the Tt-CIII$_2$ dimer. For clarity, maps were carved around the asymmetric subunits. For each protomer, density is shown in transparent grey, models in cartoon. The subunit labels indicate differences in each protomer. (**I**) UQCRSF1 head domain (magenta surface) constrained at the interface between Tt-CI and Tt-CIII$_2$. Iron sulfur (FeS) and heme co-factors (sticks) shown. (**J** and **K**) Comparison of b-hemes (J) and c-hemes (K) in respiratory CIII$_2$ and photosynthetic b_6f complex dimers across cyanobacteria PDB: 1VF5; *Mastigocladus laminosus* b_6f complex (63)) in grey, bacteria (PDB: 2YIU *P. denitrificans* (64)) in pink, yeast (PDB: 6HU9 *S. cerevisiae* (18)) in blue, plants (PDB: 7JRG *V. radiata* (20)) in green, mammals (PDB: 1BGY *B. taurus* (46)) in yellow and *T. thermophila* (orange). Hemes were superposed by one Tt-COB subunit in the dimer. Distances between hemes in Å, calculated edge-to-edge of the macrocyclic conjugated system. For clarity, only distances for *T. thermophila* and *B. taurus* are shown. (**L**) Schematic of the symmetry-broken Q cycle and Q cavity specialization of Tt-CIII$_2$. Tt-CIII protomers in dark green surface (proximal to Tt-CI Q tunnel, blue oval) or light green surface (distal to Tt-CI Q tunnel). The functional Q_N and Q_P sites are indicated with dark green ovals, corresponding to the dark green protomer. The functional UQCRSF1 head domain that is capable of a flexible swinging motion (double-headed grey arrow) is shown in dark green surface, with its FeS cluster in spheres. Both b_L and c_1 positions of the head domain are shown. Tt-CIII$_2$'s functional hemes in heteroatom-colored spheres; non-functional hemes in magenta spheres. Red crosses indicate inability of electron transfer. Tt-CI's N2 FeS cluster in spheres. Homology model of Tt-cyt c in surface colored by electrostatic potential. Approximate position of inner mitochondrial membrane marked with black lines. b_H, heme b_H; b_L, heme b_L; c_1, heme c_1; e$^-$, electron; H$^+$, proton; IMS, intermembrane space;Q, oxidized quinone; QH$_2$, reduced quinone (quinol); Q•, semiquinone.
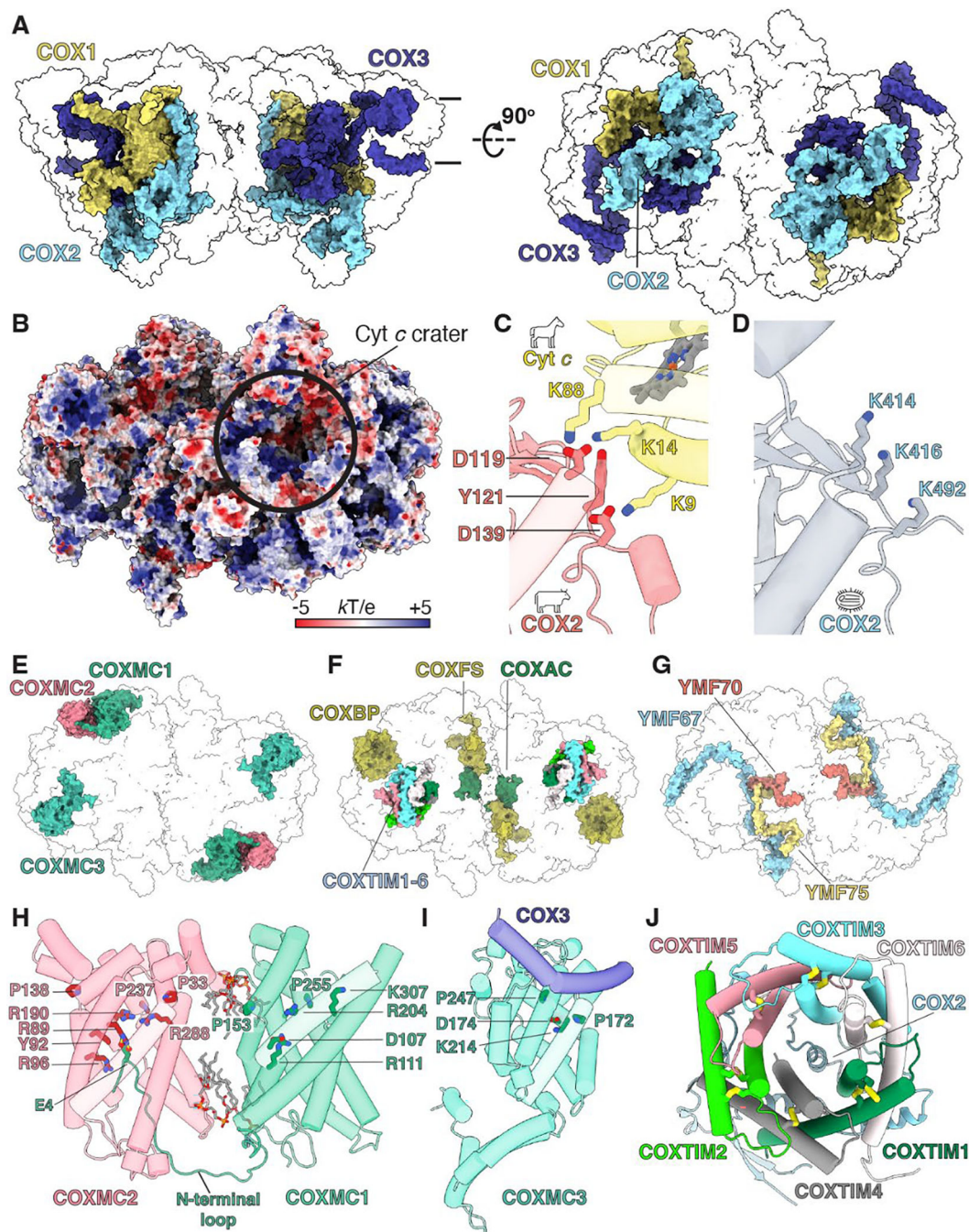
Fig. 5. Structural features of Tt-CIV$_2$.

(**A**) Structure of Tt-CIV$_2$, with core subunits in surface over silhouette of entire complex. Viewed from the membrane (left) or intermembrane space (right). (**B**) Surface electrostatic potential of Tt-CIV$_2$. Cyt c crater marked with a black circle. (**C** and **D**) Charge reversal in CIV-cyt c binding between mammals and *T. thermophila*. CIVs were aligned by COX2. Key residues in stick. (**C**) Binding of bovine COX2 (red cylinder, cow symbol) to equine cyt c (yellow cylinder, horse symbol) (PDB: 5IY5) (74). (**D**) *T. thermophila* COX2 in grey cylinder. (**E** to **G**) Notable Tt-CIV$_2$ accessory subunits viewed from IMS. (E) Mitochondrial

carrier subunits COXMC1–3. (F) Other subunits with annotated folds. (G) Mitochondrially encoded subunits YMF67, YMF70 and YMF75. (**H**) Side view of COXMC1–2 dimer (pink and green cylinders) with interfacial lipissssds (sticks). Key substrate-contacting residues, as well as conserved prolines of PX[D/E]XX[R/K] motif on odd-numbered helices in sticks. (**I**) Side view of COXMC3 (cyan cylinders) and the constraining amphipathic helix of COX3. (**J**) TIM8$_3$-TIM13$_3$-like hetero-hexamer domain with di-sulfide bonds in yellow. The Tt-specific loop of COX2 wraps around five of the COXTIM subunits and inserts itself into the central cavity of the hexamer.